Topological Ising pairing states in monolayer and trilayer TaS_2

Weipeng Chen,[1] Qingli Zhu,[1,2] Yao Zhou,[1] and Jin An[1,3,*]

[1]*National Laboratory of Solid State Microstructures and Department of Physics, Nanjing University, Nanjing 210093, China*

[2]*Department of Information Engineering, Nanjing Normal University Taizhou College, Taizhou 225300, China*

[3]*Collaborative Innovation Center of Advanced Microstructures, Nanjing University, Nanjing 210093, China*

(Received 1 April 2019; published 5 August 2019)

We study the possibility of topological superconductivity in the noncentrosymmetric monolayer and trilayer TaS_2 with out-of-plane mirror symmetry. A time-reversal-invariant nodal $(s+f)$-wave pairing state with even mirror parity is found to be a promising candidate. This mixed state holds 12 (36) nodes at the Fermi pockets around Γ for the monolayer (trilayer) case and its unconventional superconductivity is consistent with the scanning tunneling microscopy experiments observed in $2H$-TaS_2 thin flakes. Furthermore, with doping or under uniaxial pressure for trilayer $2H$-TaS_2, large-Chern-number time-reversal symmetry-breaking mixed states between $(d+id)$- and $(p-ip)$-wave pairings can be realized in the phase diagram.

DOI: 10.1103/PhysRevB.100.054503

I. INTRODUCTION

Dimensionality plays an important role in superconducting layered materials, which may behave quite differently in the two-dimensional (2D) limit. While the layered transition-metal dichalcogenide (TMD) bulk materials exhibit s-wave superconductivity [1–5], always coexisting with a competing charge density wave (CDW) [6–12], their thin flakes have been found to show many new phenomena, including spin-valley locking [13–18], the valley Hall effect [13,19–23], and Ising pairing, which is supported by a great enhancement of the in-plane upper critical magnetic field [24–29]. Recent investigations have also revealed the possibility of unconventional superconductivity in 2D TMDs [30–37].

One special member of the TMD family is $2H$-TaS_2, which has attracted much attention in recent years. In detached flakes of $2H$-TaS_2, a zero-bias conductance peak (ZBCP) was observed by scanning tunneling microscopy (STM) at 0.15 K, indicating unconventional superconductivity [38]. This leads to an f-wave pairing scenario in atomic thin $2H$-TaS_2 layers. On the other hand, it is found that the critical temperature T_c of $2H$-TaS_2 exhibits an anomalous enhancement with reduced thickness. It increases from 0.54 to about 2.1 K as the material thickness decreases from bulk to about five molecular layers [39]. Furthermore, T_c of the monolayer could reach 3 K [29]. Although this anomalous T_c-enhanced behavior is believed to result from the suppression of CDW, the vanishing of which in the 2D limit was observed by a recent experiment [40], what pairing symmetry the superconducting state in $2H$-TaS_2 thin flakes can be and whether it supports topological superconductivity remain unclear.

From the viewpoint of the crystal structure of $2H$-TaS_2, the thin flakes may behave differently for even or odd numbers of layers. Note that although the $2H$-TMD bulk always has an inversion center, only the even-layer thin films are still inversion symmetric. A recent experiment found the difference in gap structure between the trilayer and four-layer $2H$-$NbSe_2$ [41]. The odd-layer $2H$-TaS_2 thin films are noncentrosymmetric but always hold out-of-plane mirror symmetry. In this odd-layer system, the lack of inversion symmetry together with strong spin-orbit interaction could lead to novel Ising superconductivity. In this work, we will demonstrate that the Ising superconductivity in monolayer and trilayer $2H$-TaS_2 should be unconventional and even topologically nontrivial. We find a time-reversal-invariant nodal $(s+f)$-wave pairing state could be a candidate. Furthermore, the time-reversal symmetry (TRS)-breaking mixed states between $(d+id)$- and $(p-ip)$-wave pairings can be induced by doping or uniaxial pressure.

This paper is organized as follows. In Sec. II, we introduce our model. In Sec. III, we analyze the pairing symmetry and classify the gap functions according to crystal symmetry. We also include an Appendix to show the technical details of how to make use of the irreducible representations of crystal symmetry to solve the multilayer linearized gap equations. In Sec. IV, we first give the pairing phase diagram and discuss the Ising pairing states. Then we investigate the topological features of these superconducting states as well as their pairing symmetry transitions with doping or under uniaxial pressure. Finally, we summarize our results in Sec. V.

II. MODEL

TMDs have weak van der Waals couplings among TX_2 (T = Ta, Nb and X = S, Se) layers. An H-TX_2 monolayer contains three atomic ones, each of which forms a triangular lattice, with one T layer sandwiched between two X ones. The "$2H$" in $2H$-TX_2 material means the neighboring TX_2 layers in the bulk take the $AbA-CbC$ stacking sequence, preserving the global D_{6h} symmetry. The thin film we study in this paper consists of one or three TaS_2 layers. In this and the next sections we focus the discussion of model and symmetry analysis on the trilayer case, as shown schematically in

*anjin@nju.edu.cn

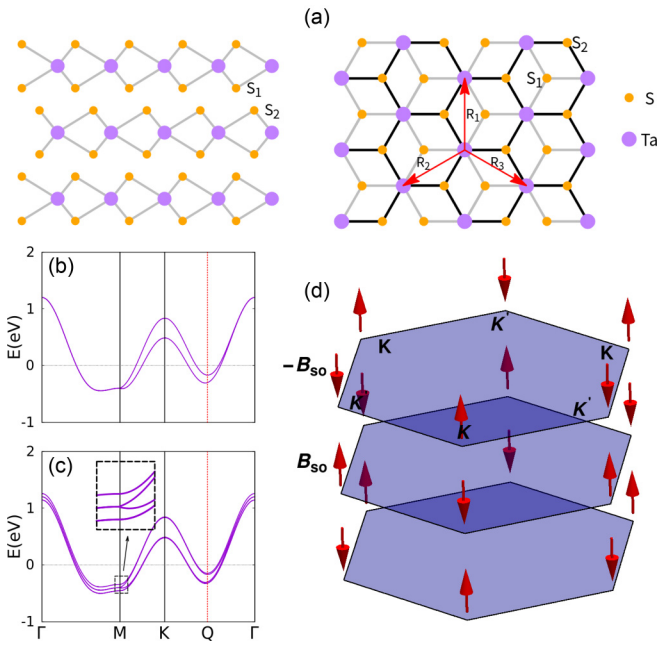

FIG. 1. (a) The side and top views of the atomic structure of trilayer $2H$-TaS_2. Three basis vectors $\boldsymbol{R}_j$ are given by the red arrows. The band structures of (b) monolayer H-TaS_2 and (c) trilayer $2H$-TaS_2. The inset is a blowup of the dotted square near M. (d) Spin-valley locking in trilayer $2H$-TaS_2, where the arrows denote the effective magnetic field B_{so} acting on the two valleys, K and K', of each layer.

Fig. 1(a), since that of the monolayer case is straightforward and parallel. We model the system by simply replacing the three TaS_2 layers by three atomic Ta layers in a *bbb* sequence because superconductivity is believed to occur only within Ta layers. Generically, a thin layer of $2H$-TaS_2 always has Fermi surface (FS) sheets centered at Γ and K (K'). Although the FS stems from d_{z^2} and d_{xy/x^2-y^2} orbitals [42–44], respectively, we simply simulate the bands by a tight-binding model based only on the d_{z^2} orbital. Here we ignore CDW as it is believed to be strongly suppressed in the thin $2H$-TaS_2 layers [39,40]. For a trilayer system, the tight-binding Hamiltonian can thus be given by

$$H_0(\boldsymbol{k}) = \begin{bmatrix} h_1(\boldsymbol{k}) & t_\perp & 0 \\ t_\perp & h_2(\boldsymbol{k}) & t_\perp \\ 0 & t_\perp & h_3(\boldsymbol{k}) \end{bmatrix}. \tag{1}$$

Here $t_\perp$ and $h_l(\boldsymbol{k})$ represent the interlayer hopping integral and the intralayer Hamiltonian for layer l ($l = 1, 2, 3$). The latter can be expressed as

$$h_l(\boldsymbol{k}) = \epsilon(\boldsymbol{k}) + h_l^{SO}(\boldsymbol{k}) + h_l^R(\boldsymbol{k}), \tag{2}$$

where $\epsilon(\boldsymbol{k}) = -\sum_{j=1}^{3}\{2t_1 \cos k_j + 2t_2 \cos(k_j - k_{j+1})\} - \mu$, with $k_j = \boldsymbol{k}\cdot\boldsymbol{R_j}$, and the unit lattice vectors $\boldsymbol{R}_1 = \boldsymbol{y}$, $\boldsymbol{R}_2 = -\boldsymbol{y}/2 - \sqrt{3}\boldsymbol{x}/2$, $\boldsymbol{R}_3 = -\boldsymbol{y}/2 + \sqrt{3}\boldsymbol{x}/2$, and $\boldsymbol{R}_4 \equiv \boldsymbol{R}_1$. Here μ is the chemical potential, and t_1 and t_2 denote the nearest-neighbor (NN) and next-nearest-neighbor hopping integrals. We fix the chemical potential $\mu = 0$ and set $(t_1, t_2, t_\perp) = (-60, -140, -40)$ meV to fit the electronic band structure from experiments and DFT calculations [39,45,46]. We notice that a smaller interlayer hopping was used in another work [29]. So a calculation with $t_\perp = -20$ meV has also been made, and the main results are found to be nearly unchanged. As depicted in Fig. 1(a), the stacking form of sulfur atoms breaks the inversion symmetry in each H-TaS_2 layer, resulting in the Ising spin-orbit coupling (SOC). Moreover, the middle TaS_2 layer can be viewed as being rotated by 180° with respect to the top or bottom molecular ones. This leads to a layer-dependent intrinsic SOC [25,47,48],

$$h_l^{SO}(\boldsymbol{k}) = (-1)^l \beta(\boldsymbol{k})\sigma_z, \tag{3}$$

where $\beta(\boldsymbol{k}) = \beta_{so}(\sin k_1 + \sin k_2 + \sin k_3)$. For electrons near K (K'), this SOC can be viewed as an effective valley-dependent out-of-plane magnetic field B_{so}, favoring spin-up (spin-down) electrons and alternating among layers, as schematically shown in Fig. 1(d). This gives rise to the well-known spin-valley locking effect [13–18]. The magnitude of B_{so} is estimated to be quite large, about 3000 T for TaS_2, since the spin splitting at K (K') is about 348 meV [45], from which β_{so} is fixed to be $\beta_{so} = 67$ meV. Ising pairing occurs when Cooper pairs are formed between electrons around K and K', spin oriented oppositely but along the out-of-plane direction. Ising superconductivity in TMDs has been supported experimentally by the significant enhancement of the in-plane upper critical magnetic field [24–29,35,49].

Rashba SOC is also taken into account. It takes the following form:

$$h_l^R(\boldsymbol{k}) = \alpha^l \boldsymbol{g}(\boldsymbol{k})\cdot\boldsymbol{\sigma}, \tag{4}$$

where $\boldsymbol{g}(\boldsymbol{k}) = (-\mathrm{Im}[\lambda(\boldsymbol{k})], -\mathrm{Re}[\lambda(\boldsymbol{k})], 0)$, with $\lambda(\boldsymbol{k}) = \sin k_1 + e^{-i\frac{2\pi}{3}}\sin k_2 + e^{-i\frac{4\pi}{3}}\sin k_3$. Since the Rashba SOC is strongly dependent on the surface normal, the coupling constants should be layer dependent and are assumed to be $(\alpha^1, \alpha^2, \alpha^3) = (\alpha_R, 0, -\alpha_R)$ for a free-standing trilayer $2H$-TaS_2, with α_R being the coupling strength. This kind of coupling also appears in the layered system with superlattice structures [50–52]. The Rashba SOC favors electron spin oriented along the in-plane directions, which means it will compete with the Ising SOC and weaken the effect of spin-valley locking and hence Ising pairing. As long as $\alpha_R \ll \beta_{so}$, Ising pairing is still expected to be dominant.

The band structures for monolayer H-TaS_2 and trilayer $2H$-TaS_2 without Rashba SOC are shown in Figs. 1(b) and 1(c), respectively. For monolayer H-TaS_2, the band is doubly degenerate at Γ but spin split at K (K'), as expected. For trilayer $2H$-TaS_2, there are four bands in total, but two of the four are doubly degenerate due to accidental degeneracy. The degeneracy can be lifted when the middle layer takes a slightly different value of β_{so} for the top and bottom layers, which still preserves the crystal symmetry of trilayer $2H$-TaS_2.

III. PAIRING INTERACTION AND SYMMETRY ANALYSIS

The monolayer and trilayer H-TaS_2 system belongs to crystal D_{3h}, while in the trilayer case, only the symmetry operations of the subgroup C_{3v} are shared by all three layers. On the other hand, it is generally thought that no interlayer pairing occurs due to the weak van der Waals force among molecular layers. Thus, the intralayer pairing basis gap functions $\Delta_i^{\Gamma,\alpha}(\boldsymbol{k})$ can be classified according to the irreducible

TABLE I. Classification of spin-singlet and spin-triplet basis gap functions based on C_{3v} symmetry, where $C(\boldsymbol{k}) = \frac{1}{\sqrt{3}}(\cos k_1 + \cos k_2 + \cos k_3)$, $C_+(\boldsymbol{k}) = \frac{1}{\sqrt{3}}(\cos k_1 + e^{i\frac{2\pi}{3}}\cos k_2 + e^{i\frac{4\pi}{3}}\cos k_3)$, $S(\boldsymbol{k}) = \frac{1}{\sqrt{3}}(\sin k_1 + \sin k_2 + \sin k_3)$, $S_+(\boldsymbol{k}) = \frac{1}{\sqrt{3}}(\sin k_1 + e^{i\frac{2\pi}{3}}\sin k_2 + e^{i\frac{4\pi}{3}}\sin k_3)$, $C_-(\boldsymbol{k}) = C_+^*(\boldsymbol{k})$, $S_-(\boldsymbol{k}) = S_+^*(\boldsymbol{k})$, with $\boldsymbol{x}_\pm = (\boldsymbol{x} \pm i\boldsymbol{y})/2$.

Γ	Singlet	Triplet
A_1	$\Psi^{A_1,on} = \frac{1}{\sqrt{2}}$	$\boldsymbol{d}^{A_1,z} = S(\boldsymbol{k})\boldsymbol{z}$
	$\Psi^{A_1,nn} = C(\boldsymbol{k})$	$\boldsymbol{d}^{A_1,xy} = i[S_-(\boldsymbol{k})\boldsymbol{x}_+ - S_+(\boldsymbol{k})\boldsymbol{x}_-]$
A_2		$\boldsymbol{d}^{A_2,xy} = S_-(\boldsymbol{k})\boldsymbol{x}_+ + S_+(\boldsymbol{k})\boldsymbol{x}_-$
E	$\begin{cases}\Psi_1^{E,nn} = C_+(\boldsymbol{k}) \\ \Psi_2^{E,nn} = C_-(\boldsymbol{k})\end{cases}$	$\begin{cases}\boldsymbol{d}_1^{E,z} = S_+(\boldsymbol{k})\boldsymbol{z} \\ \boldsymbol{d}_2^{E,z} = S_-(\boldsymbol{k})\boldsymbol{z}\end{cases}$
		$\begin{cases}\boldsymbol{d}_1^{E,xy} = \sqrt{2}S(\boldsymbol{k})\boldsymbol{x}_+ \\ \boldsymbol{d}_2^{E,xy} = -\sqrt{2}S(\boldsymbol{k})\boldsymbol{x}_-\end{cases}$
		$\begin{cases}\boldsymbol{d}_1^{E,\tilde{xy}} = \sqrt{2}S_-(\boldsymbol{k})\boldsymbol{x}_- \\ \boldsymbol{d}_2^{E,\tilde{xy}} = -\sqrt{2}S_+(\boldsymbol{k})\boldsymbol{x}_+\end{cases}$

representations (IRs) of C_{3v}, as shown in Table I. Based on whether the total spin $\hat{S}$ of the Cooper pair is 1 or 0, $\Delta_i^{\Gamma,\alpha}(\boldsymbol{k})$ takes the following two different kinds of forms:

$$\Delta_i^{\Gamma,\alpha}(\boldsymbol{k}) = \begin{cases}\Psi_i^{\Gamma,\alpha} i\sigma_y & \text{singlet pairing,} \\ \boldsymbol{d}_i^{\Gamma,\alpha}\cdot\boldsymbol{\sigma} i\sigma_y & \text{triplet pairing,}\end{cases} \tag{5}$$

where $\Psi_i^{\Gamma,\alpha}$ is the singlet order parameter and $\boldsymbol{d}_i^{\Gamma,\alpha}$ denotes the $\boldsymbol{d}$ vector for the triplet pairing. Here Γ represents the IR of C_{3v} symmetry with dimension d^Γ, and it can be $A_1(d^{A_1} = 1)$, $A_2(d^{A_2} = 1)$, or $E(d^E = 2)$. The index α is used to distinguish different types of representations in the same IR Γ, and i runs from 1 to d^Γ. As an example, for $\Gamma = A_1$, α can be *on*, *nn*, *z*, and *xy*. All these $\Delta_i^{\Gamma,\alpha}(\boldsymbol{k})$ are so normalized, $\frac{2}{N}\sum_{\boldsymbol{k}} |\Psi_i^{\Gamma,\alpha}|^2 = 1$ (or $\frac{2}{N}\sum_{\boldsymbol{k}} |\boldsymbol{d}_i^{\Gamma,\alpha}|^2 = 1$), to satisfy the following orthogonal relations between IRs:

$$\frac{1}{N}\sum_{\boldsymbol{k}} \mathrm{Tr}\{\Delta_i^{\dagger\Gamma',\alpha}(\boldsymbol{k})\Delta_j^{\Gamma,\beta}(\boldsymbol{k})\} = \delta_{\Gamma'\Gamma}\delta_{\alpha\beta}\delta_{ij}, \tag{6}$$

where N is the total number of unit cells in the system. See the Appendix for details.

Although all the basis gap functions in Table I can be realized in principle in materials with crystal C_{3v} symmetry, the in-plane triplet-pairing components such as $\boldsymbol{d}^{A_1,xy}$, $\boldsymbol{d}^{A_2,xy}$, $\boldsymbol{d}^{E,xy}$, and $\boldsymbol{d}^{E,\tilde{xy}}$ actually never occur as long as Ising pairing is dominant in $2H$-TaS_2, which is guaranteed by the strong intrinsic SOC. This is also confirmed by our numerical calculations in Sec. IV.

Without considering the pairing mechanism, the pairing term for a multilayer $2H$-TaS_2 can be generically written as

$$H_{int} = \frac{1}{2}\sum V_{s_1s_2s_3s_4}(\boldsymbol{k},\boldsymbol{k}')c_{l,\boldsymbol{k}s_1}^\dagger c_{l,-\boldsymbol{k}s_2}^\dagger \times c_{l,\boldsymbol{k}'s_3}c_{l,-\boldsymbol{k}'s_4}, \tag{7}$$

where the sum runs over the repeated indexes. $V_{s_1s_2s_3s_4}(\boldsymbol{k},\boldsymbol{k}')$ is the pairing interaction, and $c_{l,\boldsymbol{k}s}^\dagger$ is the creation operator for an electron with spin s at layer l. According to C_{3v} symmetry and taking the on-site and NN pairings into account, $V_{s_1s_2s_3s_4}(\boldsymbol{k},\boldsymbol{k}')$ can be expanded as follows:

$$\begin{aligned}V_{s_1s_2s_3s_4}(\boldsymbol{k},\boldsymbol{k}') &= v_0\Psi^{A_1,on}\Psi^{*A_1,on}(i\sigma_y)_{s_1s_2}(i\sigma_y)_{s_3s_4} \\ &+ v_1\sum_{\Gamma,i}\Psi_i^{\Gamma,nn}\Psi_i^{*\Gamma,nn}(i\sigma_y)_{s_1s_2}(i\sigma_y)_{s_3s_4} \\ &+ v_1\sum_{\Gamma,\alpha,i}[\boldsymbol{d}_i^{\Gamma,\alpha}\cdot\boldsymbol{\sigma}i\sigma_y]_{s_1s_2}[\boldsymbol{d}_i^{\Gamma,\alpha}\cdot\boldsymbol{\sigma}i\sigma_y]_{s_3s_4}^*,\end{aligned} \tag{8}$$

where v_0 (v_1) is the pairing strength for the on-site (NN) pairing interaction. Here the positive (negative) values of v_i ($i = 0, 1$) represent attractive (repulsive) interactions. In principle, each pairing channel is allowed to have a different pairing strength. However, it is hard to determine their relative ratios merely from symmetry analysis. Consequently, we treat all these NN pairing channels on the same footing and assume they share the same v_1, as most of previous works did before [30,48].

Because the trilayer $2H$-TaS_2 system lacks an inversion center, generically, there exists mixing between singlet and triplet pairings. The corresponding 6×6 pairing gap function $\Delta(\boldsymbol{k})$ for the superconducting trilayer system can thus be expanded in the basis of $\Delta_i^{\Gamma,\alpha}(\boldsymbol{k})$ as

$$\begin{aligned}\Delta(\boldsymbol{k})/\Delta &\equiv \begin{bmatrix}\Delta_{l=1}(\boldsymbol{k}) & & \\ & \Delta_{l=2}(\boldsymbol{k}) & \\ & & \Delta_{l=3}(\boldsymbol{k})\end{bmatrix} \\ &= \sum_{\alpha,i} b_i^{\Gamma,\alpha}\begin{bmatrix}\chi_{l=1,i}^{\Gamma,\alpha} & & \\ & \chi_{l=2,i}^{\Gamma,\alpha} & \\ & & \chi_{l=3,i}^{\Gamma,\alpha}\end{bmatrix}\Delta_i^{\Gamma,\alpha}(\boldsymbol{k}),\end{aligned} \tag{9}$$

where Δ is the gap value and the expansion is made only for a definite IR Γ, as mixing among different IRs is forbidden [53]. Here $\Delta_l(\boldsymbol{k})$ is the 2×2 gap matrix for layer l. The expansion coefficients $b_i^{\Gamma,\alpha}$ can be normalized as $\sum_{\alpha,i}|b_i^{\Gamma,\alpha}|^2 = 1$, while the relative pairing amplitudes $\chi_{l,i}^{\Gamma,\alpha}$ are always normalized as $\sum_l |\chi_{l,i}^{\Gamma,\alpha}|^2 = 1$. When the most energetically favorable pairing gap function $\Delta(\boldsymbol{k})$ is found, the Bogoliubov–de Gennes (BdG) Hamiltonian of this superconducting trilayer system takes the standard form

$$H_{BdG}(\boldsymbol{k}) = \begin{bmatrix}H_0(\boldsymbol{k}) & \Delta(\boldsymbol{k}) \\ \Delta^\dagger(\boldsymbol{k}) & -H_0^T(-\boldsymbol{k})\end{bmatrix}. \tag{10}$$

This D_{3h} trilayer system also has an out-of-plane mirror symmetry, with the mirror plane lying in the middle Ta layer. For the normal state, we have $[M_{xy}, H_0(\boldsymbol{k})] = 0$, with

$$M_{xy} = \begin{bmatrix}0 & 0 & 1 \\ 0 & 1 & 0 \\ 1 & 0 & 0\end{bmatrix} i\sigma_z, \tag{11}$$

which exchanges the top layer with bottom layer and reverses the in-plane spins. For the superconducting state, the mirror symmetry requires $[M^\pm, H_{BdG}(\boldsymbol{k})] = 0$, with mirror operators

$$M^\pm = \begin{pmatrix}M_{xy} & 0 \\ 0 & \pm M_{xy}^*\end{pmatrix},$$

TABLE II. Symmetry of relative pairing amplitudes $\boldsymbol{\chi}_i^{\Gamma,\alpha}$ for a pairing gap function of the trilayer $2H$-TaS_2, classified by the out-of-plane mirror symmetry.

Mirror parity	Components	$\boldsymbol{\chi}_i^{\Gamma,\alpha} \equiv (\chi_{1,i}^{\Gamma,\alpha}, \chi_{2,i}^{\Gamma,\alpha}, \chi_{3,i}^{\Gamma,\alpha})$
Even	$\psi_i^{\Gamma,\alpha}$ or $\boldsymbol{d}_i^{\Gamma,\alpha} \| z$	$\chi_{1,i}^{\Gamma,\alpha} = \chi_{3,i}^{\Gamma,\alpha}$
	$\boldsymbol{d}_i^{\Gamma,\alpha} \perp z$	$(\frac{1}{\sqrt{2}}, 0, -\frac{1}{\sqrt{2}})$
Odd	$\psi_i^{\Gamma,\alpha}$ or $\boldsymbol{d}_i^{\Gamma,\alpha} \| z$	$(\frac{1}{\sqrt{2}}, 0, -\frac{1}{\sqrt{2}})$
	$\boldsymbol{d}_i^{\Gamma,\alpha} \perp z$	$\chi_{1,i}^{\Gamma,\alpha} = \chi_{3,i}^{\Gamma,\alpha}$

leading to the requirement that

$$M_{xy}\Delta(\boldsymbol{k})M_{xy}^T = \pm\Delta(\boldsymbol{k}), \tag{12}$$

where the plus (minus) symbol represents even (odd) mirror parity [54]. Therefore, in the trilayer $2H$-TaS_2 system, the singlet components or triplet ones with $\boldsymbol{d}^\Gamma \| z$ for an even-mirror-parity state and the triplet components with $\boldsymbol{d}^\Gamma \perp z$ for an odd-mirror-parity state satisfy

$$\chi_{l=1,i}^{\Gamma,\alpha}(\boldsymbol{k}) = \chi_{l=3,i}^{\Gamma,\alpha}(\boldsymbol{k}). \tag{13}$$

The singlet components or triplet ones with $\boldsymbol{d}^\Gamma \| z$ for an odd-mirror-parity state and the triplet components with $\boldsymbol{d}^\Gamma \perp z$ for an even-mirror-parity state satisfy instead the requirements

$$\chi_{l=1,i}^{\Gamma,\alpha}(\boldsymbol{k}) = -\chi_{l=3,i}^{\Gamma,\alpha}(\boldsymbol{k}) = \frac{1}{\sqrt{2}}, \chi_{l=2,i}^{\Gamma,\alpha}(\boldsymbol{k}) = 0. \tag{14}$$

These symmetry properties are summarized in Table II.

In order to determine the detailed pairing symmetry $\Delta(\boldsymbol{k})$ and T_c of the superconducting state, we solve the following coupled linearized gap equations:

$$[\Delta_l(\boldsymbol{k})]_{s_1s_2} = \frac{-T_c}{N}\sum_{\omega_n\boldsymbol{k}'s_3s_4} V_{s_1s_2s_3s_4}(\boldsymbol{k},\boldsymbol{k}') \times [G(k')\Delta(\boldsymbol{k}')G^\tau(-k')]_{\substack{l,l\\ s_3s_4}}, \tag{15}$$

where $G(k) = [i\omega_n - H_0(\boldsymbol{k})]^{-1}$ is the Matsubara Green's function for the normal state, with $k \equiv (\boldsymbol{k}, i\omega_n)$. By solving the above eigenequation for each IR Γ, one obtains its eigenstates and corresponding T_c. The most favorable pairing state just corresponds to the eigenstate with the highest T_c. See the Appendix for details.

IV. RESULTS AND DISCUSSION

A. Monolayer H-TaS_2 and trilayer $2H$-TaS_2

We first study the superconducting state for the monolayer H-TaS_2 without Rashba SOC. This monolayer system preserves the out-of-plane mirror symmetry $i\sigma_z$, which has a requirement for the $\boldsymbol{d}$ vectors $\boldsymbol{d}^\Gamma$ of the triplet components: $\boldsymbol{d}^\Gamma$ is either parallel or normal to the TaS_2 plane, as shown in Table I. When $\boldsymbol{d}^\Gamma \| z$ ($\boldsymbol{d}^\Gamma \perp z$), the mirror parity of the superconducting state is even (odd). Thus, in this noncentrosymmetric monolayer system, the singlet components can be mixed merely with the triplet components having $\boldsymbol{d}^\Gamma \| z$ to form an even-mirror-parity state, while the odd-mirror-parity state is a pure triplet state consisting of only components with $\boldsymbol{d}^\Gamma \perp z$. The odd-mirror-parity state can be ruled out as Ising pairing is dominant due to strong Ising SOC. Figure 2(a) is the pairing phase diagram calculated for the monolayer H-TaS_2. One finds two even-mirror-parity states, both of which are mixed: the mixed state between $\Psi^{A_1,nn}$ and $\boldsymbol{d}^{A_1,z}$ and that between $\Psi^{A_1,on}$ and $\Psi^{A_1,nn}$. The latter is a topologically trivial s-wave state, which is fully gapped on all the FSs, while the former could be topologically nontrivial since $\boldsymbol{d}^{A_1,z}$ is an $\hat{S}_z = 0$ f-wave pairing, which holds three nodal lines.

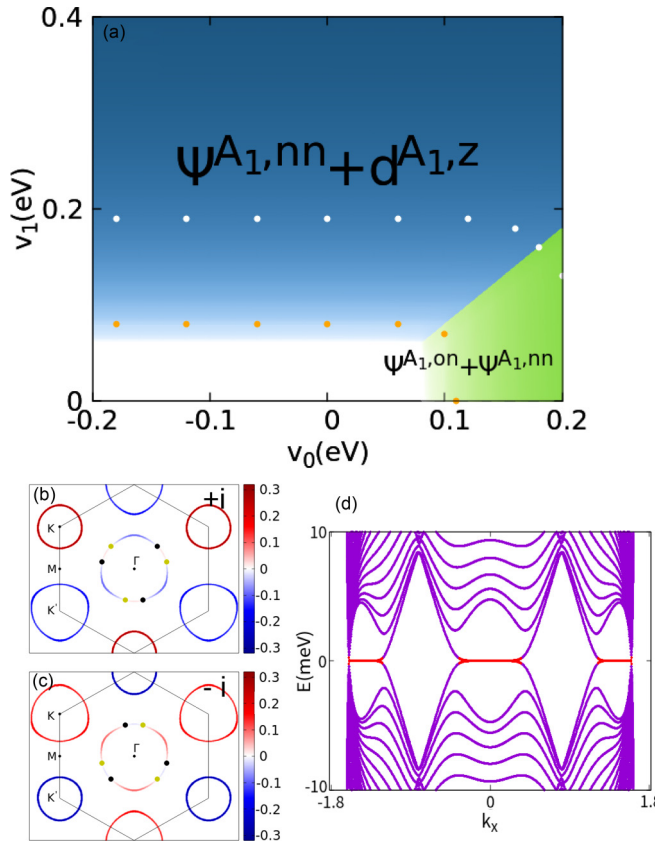

FIG. 2. (a) v_0 versus v_1 pairing phase diagram of monolayer H-TaS_2, where the white (orange) dots show the equal T_c line with $T_c = 10$ K (1×10^{-2} K). The FS and nodes of (b) sector $+i$ and (c) sector $-i$ for the $\boldsymbol{d}^{A_1,z} + \Psi^{A_1,nn}$ state. The FSs are colored in red (blue) to represent the positive (negative) gap functions. The black (yellow) dots denote the nodes with winding number $+1$ (-1). Parameters are chosen to be $(v_0, v_1) = (0.1, 0.16)$ eV, $(\Delta^s, \Delta^f) = \Delta(-0.252, 0.968)$, with $\Delta \approx 1$ K. (d) The corresponding edge band for sector $+i$ with open-boundary conditions along the y direction, where for a better view, Δ has been enlarged 20 times without changing the topological nature of the system.

To investigate the topological feature of the $\Psi^{A_1,nn} + \boldsymbol{d}^{A_1,z}$ state, which can be favorable when the NN pairing is dominant, one can block diagonalize the monolayer Hamiltonian into $\pm i$ (mirror parity) sectors according to the mirror symmetry [55],

$$H_{BdG}(\boldsymbol{k}) \to \begin{bmatrix} H_{+i}(\boldsymbol{k}) & 0 \\ 0 & H_{-i}(\boldsymbol{k}) \end{bmatrix}.$$

The two Hamiltonians are connected to each other by TRS: $H_{-i}(\boldsymbol{k}) = H_{+i}(-\boldsymbol{k})$. The excitation spectrum

TABLE III. Detailed expansion coefficients for the four representative mixed pairing states of IR A_1 denoted by P and Q in Fig. 3(a) and R and T in Fig. 4(a). These coefficients are obtained from the orthogonal relations and Eqs. (A6) and (A7) in the Appendix.

State	$b^{A_1,on}$; $\chi^{A_1,on}$	$b^{A_1,nn}$; $\chi^{A_1,nn}$	$b^{A_1,z}$; $\chi^{A_1,z}$	$b^{A_1,xy}$; $\chi^{A_1,xy}$
P		0.179; (−0.642, 0.419, −0.642)	0.983; (0.586, 0.560, 0.586)	
Q	0.990; (0.572, 0.584, 0.572)	−0.044; (0.570, 0.580, 0.570)		
R		0.151; (−0.627, 0.455, −0.627)	0.892; (0.583, 0.566, 0.583)	−0.424(0.707, 0, −0.707)
T	0.967; (0.595, 0.539, 0.595)	0.100; (−0.570, −0.580, −0.570)		−0.225(0.707, 0, −0.707)

is $E_{+i}(\boldsymbol{k}) = \sqrt{[\epsilon(\boldsymbol{k}) - \beta(\boldsymbol{k})]^2 + [\Delta^f(\boldsymbol{k}) + \Delta^s(\boldsymbol{k})]^2}$, $E_{-i}(\boldsymbol{k}) = E_{+i}(-\boldsymbol{k})$, with $\Delta^f(\boldsymbol{k}) = \Delta^f S(\boldsymbol{k})$ and $\Delta^s(\boldsymbol{k}) = \Delta^s C(\boldsymbol{k})$. Here $(\Delta^s, \Delta^f) = \Delta(b^{A_1,nn}, b^{A_1,z})$, which are found to take real values. There are 12 nodal points, and all nodes are located at the Fermi pockets around Γ, while the superconducting state is fully gapped, with its order parameter taking opposite signs at the Fermi pockets around K and K' [see Figs. 2(b) and 2(c)]. Because the superconducting state is chiral symmetric, each node is characterized by a winding number (WN). It can be calculated via

$$\nu_{\pm i} = \frac{1}{2\pi i}\oint dk \mathrm{Tr}\partial_k \ln q_{\pm i}(\boldsymbol{k}), \tag{16}$$

where the integration is along any small loop around the node and $q_{\pm i}(\boldsymbol{k}) = i[\Delta^f(\boldsymbol{k}) \pm \Delta^s(\boldsymbol{k})] + [\epsilon(\boldsymbol{k}) \mp \beta(\boldsymbol{k})]$ appears in the off-diagonal representation of $H_{\pm i}(\boldsymbol{k})$:

$$H_{\pm i}(\boldsymbol{k}) \to \begin{bmatrix} 0 & q_{\pm i}(\boldsymbol{k}) \\ q^\dagger_{\pm i}(\boldsymbol{k}) & 0 \end{bmatrix}.$$

The edge states calculated for H_{+i} with a zigzag boundary shown in Fig. 2(d) give the Majorana flat edge band lying between the projections of pairs of nodes with opposite WNs.

Now we turn to study the superconducting state in trilayer $2H$-TaS_2. Its pairing phase diagram is illustrated in Fig. 3(a), which is similar to that of the monolayer H-TaS_2: There are two mixed Ising pairing states, including a trivial full-gap s-wave state and a topologically nontrivial mixed one between $\Psi^{A_1,nn}$ and $\boldsymbol{d}^{A_1,z}$. The $\Psi^{A_1,nn} + \boldsymbol{d}^{A_1,z}$ state is dominated by the f-wave triplet component $\boldsymbol{d}^{A_1,z}$, and the expansion coefficients for a representative state in the phase diagram are given in Table III. As before, we block diagonalize the mirror-symmetric $H_{BdG}(\boldsymbol{k})$ into two TRS connected sectors $H_{\pm i}(\boldsymbol{k})$. Due to $\hat{S}_z$ conservation, $H_{+i}(\boldsymbol{k})$ can be further reduced by a basis change to two smaller sectors I and II:

$$H_{+i}(\boldsymbol{k}) \to \begin{bmatrix} H^I_{+i}(\boldsymbol{k}) & 0 \\ 0 & H^{II}_{+i}(\boldsymbol{k}) \end{bmatrix},$$

with

$$H^I_{+i}(\boldsymbol{k}) = \begin{bmatrix} \epsilon(\boldsymbol{k}) + \beta(\boldsymbol{k}) & \Delta^f_1(\boldsymbol{k}) - \Delta^s_1(\boldsymbol{k}) \\ \Delta^f_1(\boldsymbol{k}) - \Delta^s_1(\boldsymbol{k}) & -\epsilon(\boldsymbol{k}) - \beta(\boldsymbol{k}) \end{bmatrix}, \tag{17}$$

$$H^{II}_{+i}(\boldsymbol{k}) = \begin{bmatrix} \epsilon(\boldsymbol{k}) - \beta(\boldsymbol{k}) & \sqrt{2}t_\perp & 0 & \Delta^f_2(\boldsymbol{k}) + \Delta^s_2(\boldsymbol{k}) \\ \sqrt{2}t_\perp & \epsilon(\boldsymbol{k}) + \beta(\boldsymbol{k}) & \Delta^f_1(\boldsymbol{k}) + \Delta^s_1(\boldsymbol{k}) & 0 \\ 0 & \Delta^f_1(\boldsymbol{k}) + \Delta^s_1(\boldsymbol{k}) & -\epsilon(\boldsymbol{k}) + \beta(\boldsymbol{k}) & -\sqrt{2}t_\perp \\ \Delta^f_2(\boldsymbol{k}) + \Delta^s_2(\boldsymbol{k}) & 0 & -\sqrt{2}t_\perp & -\epsilon(\boldsymbol{k}) - \beta(\boldsymbol{k}) \end{bmatrix}. \tag{18}$$

Here $H^{I(II)}_{+i}(\boldsymbol{k})$ are written in the bases of $(c_{-,\boldsymbol{k}\downarrow}, c^\dagger_{-,-\boldsymbol{k}\uparrow})$ and $(c_{+,\boldsymbol{k}\uparrow}, c_{2,\boldsymbol{k}\uparrow}, c^\dagger_{+,-\boldsymbol{k}\downarrow}, c^\dagger_{2,-\boldsymbol{k}\downarrow})$, respectively, with $c_{\pm,\boldsymbol{k}\sigma} = \frac{1}{\sqrt{2}}(c_{1,\boldsymbol{k}\sigma} \pm c_{3,\boldsymbol{k}\sigma})$. $H^{I(II)}_{-i}(\boldsymbol{k})$ can be derived according to the TRS as we mentioned above: $H_{-i}(\boldsymbol{k}) = H_{+i}(-\boldsymbol{k})$. For a definite band n, the superconducting state on its FS can be described by the effective gap function or the projected gap, which is given by the diagonal entry $\widetilde{\Delta}_{n,n}(\boldsymbol{k})$. Here the effective gap function $\widetilde{\Delta}(\boldsymbol{k})$ is given by $\widetilde{\Delta}(\boldsymbol{k}) = U^\dagger(\boldsymbol{k})\Delta(\boldsymbol{k})U^*(-\boldsymbol{k})$. The unitary matrix $U(\boldsymbol{k})$ diagonalizes $H_0(\boldsymbol{k})$: $U^\dagger(\boldsymbol{k})H_0(\boldsymbol{k})U(\boldsymbol{k}) = D(\boldsymbol{k})$, with $D(\boldsymbol{k})$ being a diagonal matrix. At the FS around K or K', the superconducting state is fully gapped, and the projected gap takes positive and negative values alternatively, as shown in Fig. 3(b). The same reason leads to the existence of nodes at the FS around Γ. Around each FS, the sign of the projected gap changes six times, and there are 6 (12) nodes for $H^I_{+i}(\boldsymbol{k})$ ($H^{II}_{+i}(\boldsymbol{k})$) and 36 nodes in total for $H_{BdG}(\boldsymbol{k})$. Since both $H^I_{+i}(\boldsymbol{k})$ and $H^{II}_{+i}(\boldsymbol{k})$ hold chiral symmetry, each node has a well-defined WN ±1, as exhibited in Fig. 3(b).

Taking the empirical temperature-dependent upper critical magnetic field of thin layer $2H$-TaS_2, which cannot be explained by a pure singlet or triplet pairing, into account [29], the nodal $(s+f)$-wave pairing state mentioned above can be a promising candidate. It is evident that the Majorana flat band of the Andreev bound states of such a time-reversal-invariant nodal superconductor will give rise to a zero-energy peak of the density of states. This is consistent with the recent STM experiment on superconducting $2H$-TaS_2 detached flakes [38,56], where a ZBCP was indeed observed.

In the above discussion, the Rashba SOC has been neglected for simplicity. If a relatively small α_R is taken into account, the above main results are qualitatively unchanged. However, if α_R is assumed to be sufficiently large, a $\boldsymbol{d}^{A_1,xy}$ pairing component is expected to be induced since the Rashba SOC favors the triplet pairing with $\boldsymbol{d}^\Gamma \perp \boldsymbol{z}$. A detailed

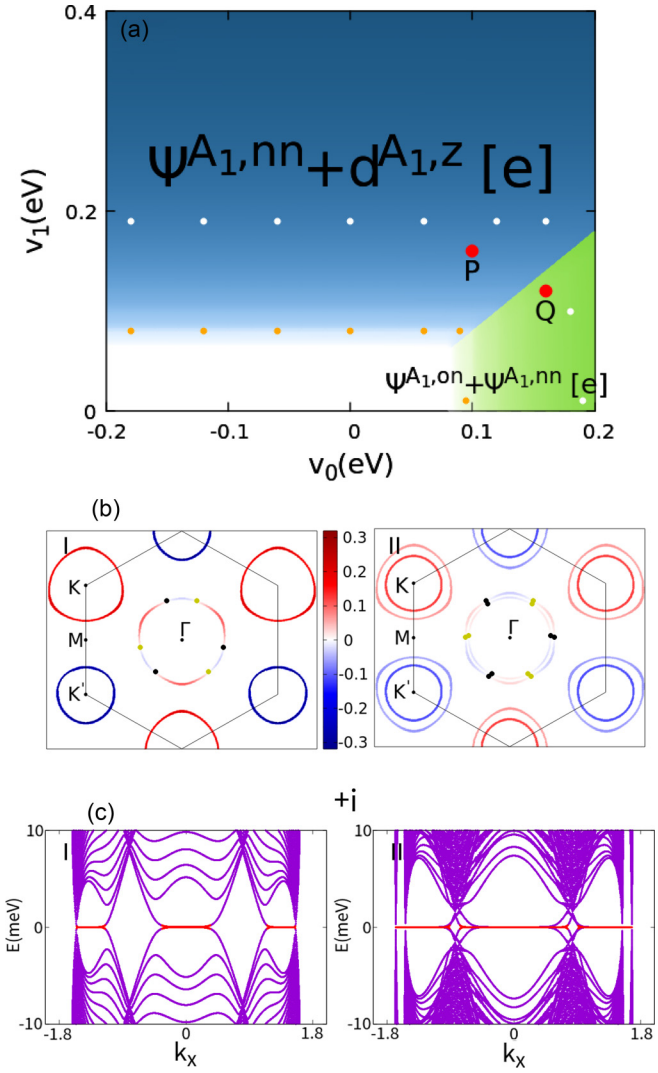

FIG. 3. (a)The same as Fig. 2, except for trilayer $2H$-TaS_2. The symbol "e" represents even mirror parity. (b) The FS and nodes of sector $+i$ for the representative mixed state denoted by P in (a), shown for the two subsectors. Here the gap value is chosen to be $\Delta \approx 1$ K. (c) The corresponding edge band for sector $+i$.

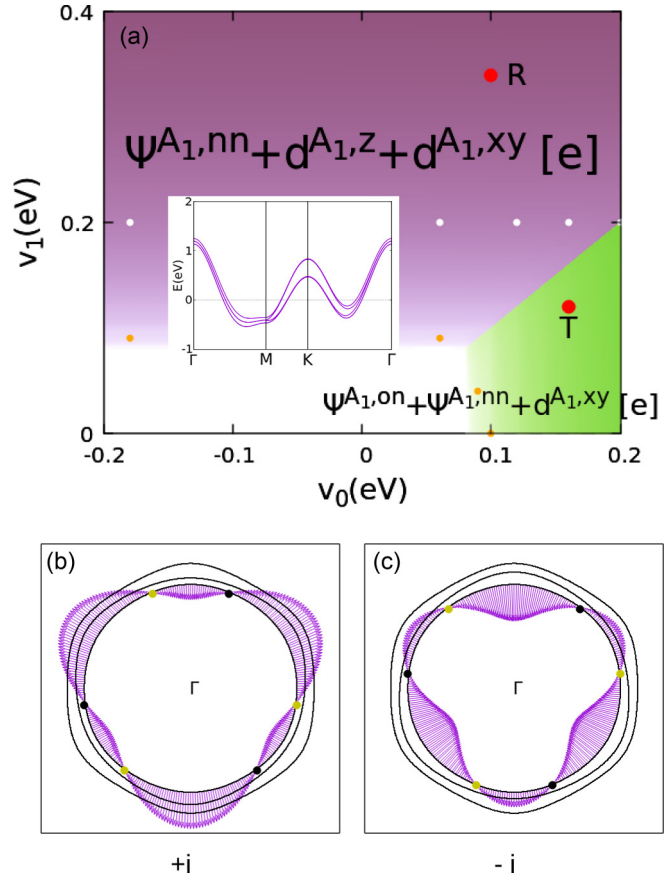

FIG. 4. (a) The pairing phase diagram with strong Rashba SOC $\alpha_R = 50$ meV. The inset is the corresponding band structure. The FS around Γ of (b) sector $+i$ and (c) sector $-i$ for the representative new mixed state denoted by R in (a). The arrows represent the projected gap functions $\tilde{\Delta}_{n,n}(\boldsymbol{k})$ on the innermost FS, with their lengths (angles) denoting the absolute values (phases) of $\tilde{\Delta}_{n,n}(\boldsymbol{k})$. The black (yellow) dots represent the nodes with WN $+1$ (-1).

calculation confirms this point and gives the pairing phase diagram shown in Fig. 4(a) for α_R up to 50 meV, which is so large that it is competing with the intrinsic SOC and hence strongly suppressing Ising pairing. Here $\hat{S}_z$ conservation is violated, so neither $H_{+i}(\boldsymbol{k})$ nor $H_{-i}(\boldsymbol{k})$ could be block diagonalized as before. This system with strong Rashba SOC is found to be still gapless but with a reduced number of nodes: All the FS sheets are fully gapped except the two innermost ones around Γ, each of which has six nodes, as depicted in Figs. 4(b) and 4(c), respectively.

B. Doping and pressure effects of trilayer $2H$-TaS_2

The superconducting behavior can be significantly tuned by doping. Experimentally, the bulk TMDs can be chemically doped with Na and Cu or electron doped by the substrate [57–60], while the thin films on a substrate can also be effectively doped by a gate voltage [24,28,61]. Here in the trilayer $2H$-TaS_2, we assume a rigid band and consider the effect of p-type doping by fixing the chemical potential $\mu = -100$ meV, which is near the Van Hove singularity (VHS) at Q [shown in Fig. 1(c)] and M.

Figure 5(a) gives the pairing phase diagram, where a new even-mirror-parity mixed phase $\Psi^{E,nn} + \boldsymbol{d}^{E,z}$ of the IR E appears. Because the IR E is 2D, in this mixed state any combination between $\Psi_1^{E,nn}$ and $\Psi_2^{E,nn}$ (or $\boldsymbol{d}_1^{E,z}$ and $\boldsymbol{d}_2^{E,z}$) is allowed and shares identical T_c determined by Eq. (15). In order to determine which combination is the most energetically favorable, one can make an energy minimization, which leads to a TRS-breaking mixed state between $(d + id)$-wave [$(d - id)$-wave] and $(p - ip)$-wave [$(p + ip)$-wave] pairings. The detailed expansion coefficients for a representative state of this phase are given in Table IV. This mixed Ising pairing phase is fully gapped. As an example, Fig. 5(c) shows the projected gap functions on the FS. A mirror Chern number(MCN) $C_{\pm i}$ can be defined for each sector $H_{\pm i}(\boldsymbol{k})$. More conveniently, MCN $C_{\pm i}^{I(II)}$ is also meaningful for each subsector $H_{\pm i}^{I(II)}(\boldsymbol{k})$, as total spin $\hat{S}_z$ is still conserved in the superconducting state. In the weak-coupling limit, each MCN can actually be viewed as the sum over the phase WNs of the projected order parameter

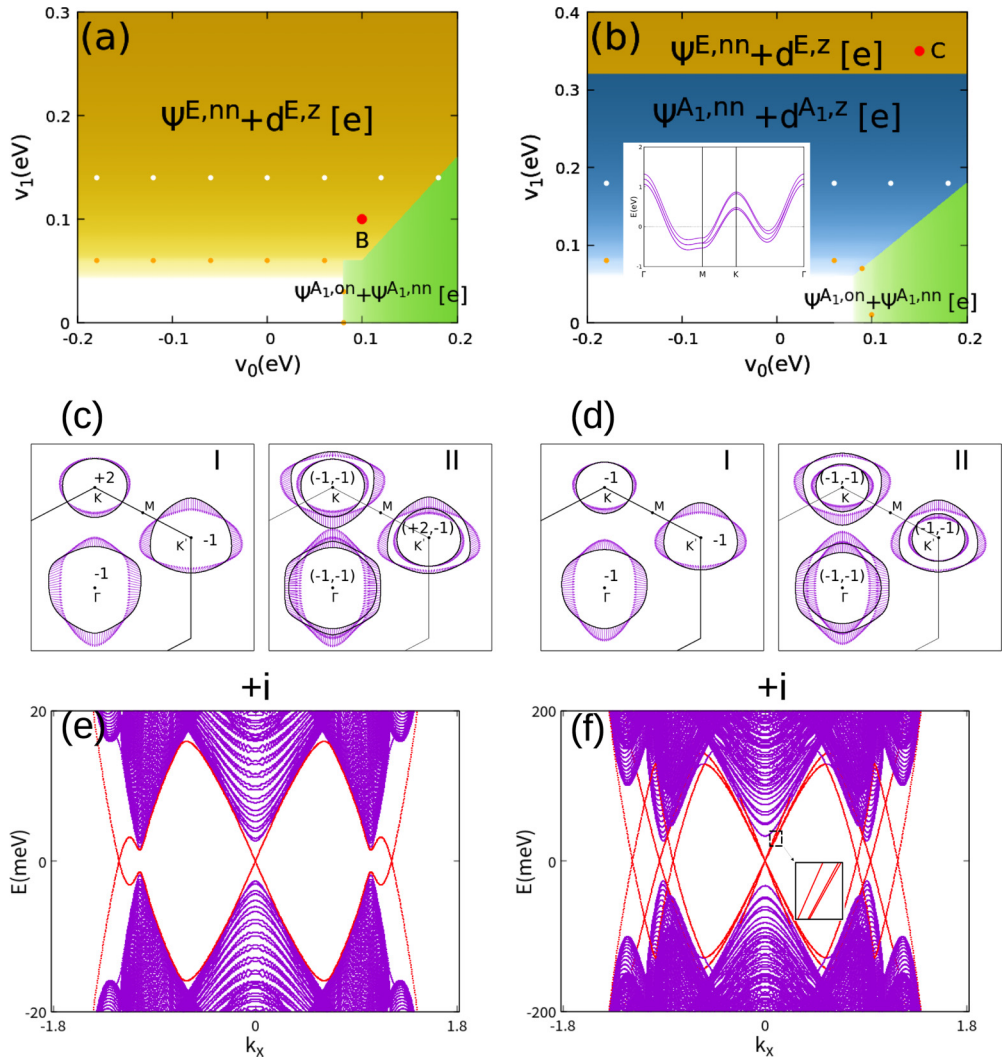

FIG. 5. (a) and (b) v_0 versus v_1 pairing phase diagram for the hole-doped and uniaxially compressed trilayer $2H$-TaS_2, respectively. In (a), the chemical potential μ is set to be -100 meV, while in (b) $t_\perp$ is set to be -90 meV with the carrier density being unchanged. The inset of (b) gives the band structure under uniaxial pressure along the z axis. (c) and (d)The FS of sector $+i$ for a representative $\boldsymbol{d}^{E_1,nn}+\Psi^{E_1,z}$ state denoted by B in (a) and by C in (b). The number on each FS denotes the phase WN of $\widetilde{\Delta}_{n,n}$. The expansion coefficients for the gap function take values in Table IV, and the gap value is chosen to be $\Delta \approx 1$ K for B and 200 K for C. (e) and (f) The corresponding edge band for sector $+i$ with the open-boundary conditions along the y axis, where for a better view, the gap value in (e) has been enlarged 20 times.

$\widetilde{\Delta}_{n,n}(\boldsymbol{k})$ on each FS, as depicted in Fig. 5(c). Here we have a new WN defined on the nth Fermi pocket γ:

$$\nu_n = \frac{1}{2\pi i}\oint_\gamma dk\partial_k ln\widetilde{\Delta}_{n,n}(\boldsymbol{k}), \tag{19}$$

with the loop integral along the FS. Therefore, the total Chern number of the trilayer $2H$-TaS_2 is -6, namely, $(C_{+i}, C_{-i}) = (-3, -3)$, which is consistent with the corresponding chiral edge states of H_{+i} shown in Fig. 5(e).

The induced $(d+p)$-wave superconductivity can be qualitatively understood as follows. The gap functions $C_+(\boldsymbol{k})$ $(d+id$ wave) and $S_+(\boldsymbol{k})$ $(p-ip$ wave) maximize at saddle point M and near saddle point Q, respectively, while the maximum amplitudes of gap functions $C(\boldsymbol{k})$ (extended s wave) and $S(\boldsymbol{k})$ (f wave) are located at Γ and K. Under p-type doping, the Fermi level will approach VHS at M and Q; consequently, the $(d+p)$-wave pairing will dominate the NN pairing channels. On the contrary, n-type doping raises

TABLE IV. Detailed expansion coefficients for the representative mixed pairing states of the 2D IR E corresponding to points B and C in Figs. 5(a) and 5(b). These coefficients are obtained from the orthogonal relations and Eqs. (A6) and (A7) in the Appendix.

State	$b_1^{E,nn}$; $\boldsymbol{\chi}_1^{E,nn}$	$b_2^{E,nn}$; $\boldsymbol{\chi}_2^{E,nn}$	$b_1^{E,z}$; $\boldsymbol{\chi}_1^{E,z}$	$b_2^{E,z}$; $\boldsymbol{\chi}_2^{E,z}$
B	0.285; (−0.637, 0.434,−0.637)		0.958; (0.571, 0.589, 0.571)	
C	0.182; (−0.665, 0.341, −0.665)		0.983; (0.564, 0.602, 0.564)	

the Fermi level, and the Fermi pockets will shrink to Γ and K. An $(s+f)$-wave pairing similar to the undoped case is thus expected and has been confirmed by our calculation. The above rough description just demonstrates why $(d \pm id)$- and $(p \mp ip)$-wave pairings could be favored under p-type doping. However, how these pairings are mixed and their mixing coefficients are determined from symmetry and the linearized gap equation (15).

On the other hand, since the couplings between TaS_2 layers are weak van der Waals forces, uniaxial pressure can also be applied to tune the features of the material. The pressure dependences of T_c in $2H$-TMDs were measured recently [60, 62–65]. Here we assume that the only effect of the uniaxial pressure along the z axis is the enhancement of interlayer coupling $t_\perp$. We set $t_\perp = -90$ meV here and get the pairing diagram shown in Fig. 5(b). There are three mixed phases. Except for the trivial one, both the gapless $\Psi^{A_1,nn} + \boldsymbol{d}^{A_1,z}$ and fully gapped $\Psi_1^{E,nn} + \boldsymbol{d}_1^{E,z}$ phases appear. Similar to the doping case, the $\Psi_1^{E,nn} + \boldsymbol{d}_1^{E,z}$ state under pressure is gapful and TRS-breaking but takes a different Chern number, indicating it is topologically different from that in Fig. 5(a). In detail, the MCNs of the two subsectors here are $C_{+i}^{I} = -3$ and $C_{+i}^{II} = -6$ [see Fig. 5(d)]. The total Chern number is thus -18, as $C_{+i} = C_{-i} = -9$, consistent with the corresponding current-carrying chiral edge states of $H_{+i}(\boldsymbol{k})$ shown in Fig. 5(f). This mixed pairing phase has a rather high T_c (about 200 K) and is expected to be possibly realized by high-pressure experiments on $2H$-TaS_2 thin flakes.

V. CONCLUSION

In summary, based on the linearized gap equation and symmetry analysis, we have obtained the pairing phase diagram of the monolayer and trilayer Ising superconductor TaS_2 and found a nodal $(s+f)$-wave state. We suggest that this nodal pairing could be responsible for the anomalous tunneling conductance observed in STM experiments. The nodal structure is so robust that even a strong mirror-symmetric Rashba SOC (up to 50 meV) cannot fully gap the system. In addition, both p-type doping and uniaxial pressure along the z axis could induce large-Chern-number TRS-breaking mixed states between $(d+id)$- and $(p-ip)$-wave pairings. Our result indicates that the superconducting trilayer $2H$-TaS_2 could be a promising candidate for realization of topological superconductors. This study will be helpful to understand the unconventional superconductivity in thin-layer $2H$-TaS_2 and other 2D TMDs. However, final determination of the pairing symmetry of these 2D Ising superconductors requires more theoretical and experimental efforts.

ACKNOWLEDGMENTS

We thank J. P. Xiao and F. Xiong for useful discussions. This work is supported by NSFC Project No. 111774126 and 973 Project No. 2015CB921202.

APPENDIX

In this Appendix we first prove the orthogonal relations (6) and then show in detail how to solve the eigenequation (15) for a definite IR Γ and obtain its T_c and pairing gap function $\Delta(\boldsymbol{k})$ for a multilayer superconductor.

To prove Eq. (6), we define $f_{ij}(\Gamma, \alpha, \Gamma', \beta)$ as follows:

$$\begin{aligned} & f_{ij}(\Gamma, \alpha, \Gamma', \beta) \\ & \equiv \sum_{\boldsymbol{k}} \mathrm{Tr}\left\{\Delta_i^{\Gamma,\alpha}(\boldsymbol{k})\Delta_j^{\dagger\Gamma',\beta}(\boldsymbol{k})\right\} \\ & = \sum_{\boldsymbol{k}} \mathrm{Tr}\left\{D^\dagger(R)\Delta_i^{\Gamma,\alpha}(\boldsymbol{k})D^*(R)D^\tau(R)\Delta_j^{\dagger\Gamma',\beta}(\boldsymbol{k})D(R)\right\} \\ & = \frac{1}{g}\sum_{R,m,n,\boldsymbol{k}} D_{im}^{\Gamma}(R)D_{jn}^{*\Gamma'}(R)\mathrm{Tr}\left\{\Delta_m^{\Gamma,\alpha}(R^{-1}\boldsymbol{k})\Delta_n^{\dagger\Gamma',\beta}(R^{-1}\boldsymbol{k})\right\} \\ & = \sum_{m,n}\frac{1}{d^\Gamma}\delta_{ij}\delta_{mn}\delta_{\Gamma\Gamma'}f_{m,n}(\Gamma, \alpha, \Gamma', \beta) \\ & = \delta_{ij}\frac{1}{d^\Gamma}\sum_m f_{m,m}(\Gamma, \alpha, \Gamma, \beta), \end{aligned} \tag{A1}$$

where g is the order of the symmetry group G of the system and R is a group element, with $D(R)$ being its 2×2 spin-rotation representation. The orthogonal relation between different IRs has been used here in the derivation. Remarkably, $f_{ii}(\Gamma, \alpha, \Gamma, \beta)$ is independent of i. Moreover, for $\alpha \neq \beta$ in the same Γ, $f_{ii}(\Gamma, \alpha, \Gamma, \beta)$ is generically zero, so one has

$$f_{ij}(\Gamma, \alpha, \Gamma', \beta) = \delta_{\Gamma\Gamma'}\delta_{\alpha\beta}\delta_{ij}f(\Gamma, \alpha), \tag{A2}$$

where the positive number $f(\Gamma, \alpha) \equiv f_{ii}(\Gamma, \alpha, \Gamma, \alpha)$ can be renormalized to be 1 if $\Delta_i^{\Gamma,\alpha}(\boldsymbol{k})$ has been properly normalized. Thus, we come to the orthogonal relations of Eq. (6). These orthogonal relations can also be rewritten as

$$\frac{2}{N}\sum_{\boldsymbol{k}} \Psi_i^{\Gamma,\alpha}\Psi_j^{*\Gamma',\beta} = \delta_{\Gamma\Gamma'}\delta_{\alpha\beta}\delta_{ij}, \tag{A3}$$

$$\frac{2}{N}\sum_{\boldsymbol{k}} \boldsymbol{d}_i^{\Gamma,\alpha}\cdot\boldsymbol{d}_j^{*\Gamma',\beta} = \delta_{\Gamma\Gamma'}\delta_{\alpha\beta}\delta_{ij}, \tag{A4}$$

which can be easily confirmed by checking Table I for crystal C_{3v}.

Now by making use of the above orthogonal relations we try to solve Eq. (15) for a multilayer system. Multiplying the two sides of the equation by $[\Delta_i^{*\Gamma,\alpha}(\boldsymbol{k})]_{s_1,s_2}$, then taking the trace over spin indexes and making a sum over $\boldsymbol{k}$, one has

$$\begin{aligned} & \frac{1}{N}\sum_{\boldsymbol{k}} \mathrm{Tr}\left\{\Delta_i^{\dagger\Gamma,\alpha}(\boldsymbol{k})\Delta_l(\boldsymbol{k})\right\} \\ & = \frac{-T_c}{N^2}\sum_{\omega_n,\boldsymbol{k}s_1s_2}\left[\Delta_i^{*\Gamma,\alpha}(\boldsymbol{k})\right]_{s_1s_2} \\ & \quad \times \sum_{\boldsymbol{k}'s_3s_4} V_{s_1s_2s_3s_4}(\boldsymbol{k},\boldsymbol{k}')[G(k')\Delta(\boldsymbol{k}')G^\tau(-k')]_{\substack{l,l\\ s_3s_4}} \\ & = \frac{-T_c}{N^2}\sum_{\omega_n,\boldsymbol{k}s_1s_2}\left[\Delta_i^{*\Gamma,\alpha}(\boldsymbol{k})\right]_{s_1s_2} \\ & \quad \times \sum_{\substack{\boldsymbol{k}'s_3s_4\\ \Gamma',\beta,j}} v^{\Gamma',\beta}\left[\Delta_j^{\Gamma',\beta}(\boldsymbol{k})\right]_{s_1s_2}\left[\Delta_j^{*\Gamma',\beta}(\boldsymbol{k}')\right]_{s_3s_4} \\ & \quad \times [G(k')\Delta(\boldsymbol{k}')G^\tau(-k')]_{\substack{l,l\\ s_3s_4}} \end{aligned}$$

$$= \frac{-T_c}{N^2} \sum_{\omega_n, \boldsymbol{k}', \Gamma', \beta} v^{\Gamma', \beta} \mathrm{Tr}\left\{ \Delta_i^{\dagger \Gamma', \beta}(\boldsymbol{k}') \left[G(k') \Delta(\boldsymbol{k}') G^{\tau}(-k') \right]_{l,l} \right\}$$
$$\times \sum_{\boldsymbol{k}} \mathrm{Tr}\{ \Delta_i^{\dagger \Gamma, \alpha}(\boldsymbol{k}) \Delta_i^{\Gamma', \beta}(\boldsymbol{k}) \}$$
$$= \frac{-T_c}{N} \sum_{\omega_n, \boldsymbol{k}'} v^{\Gamma, \alpha} \mathrm{Tr}\left\{ \left[G(k') \Delta(\boldsymbol{k}') G^{\tau}(-k') \right]_{l,l} \Delta_i^{\dagger \Gamma, \alpha}(\boldsymbol{k}') \right\}$$
$$= \frac{-T_c}{N} \sum_{\omega_n, \boldsymbol{k}} v^{\Gamma, \alpha} \mathrm{Tr}\{ [G(k) \Delta(\boldsymbol{k}) G^{\tau}(-k)]_{l,l} \Delta_i^{\dagger \Gamma, \alpha}(\boldsymbol{k}) \}, \quad \text{(A5)}$$

where N is the total number of unit cells of the system. Substituting the expansion of $\Delta(\boldsymbol{k})$ [Eq. (9)] into the above equation, one has a simplified version of the eigenequation,

$$a_{l,i}^{\Gamma, \alpha} = \sum_{l' \beta} Q_{l,l'}^{\Gamma, \alpha\beta} a_{l',i}^{\Gamma, \beta}, \quad \text{(A6)}$$

where $a_{l,i}^{\Gamma, \alpha} = b^{\Gamma, \alpha} \chi_{l,i}^{\Gamma, \alpha}$. $Q_{l,l'}^{\Gamma, \alpha\beta}$ is independent of i and reads

$$Q_{l,l'}^{\Gamma, \alpha\beta} = \frac{-T_c v^{\Gamma, \alpha}}{N} \sum_{\beta, \boldsymbol{k}, \omega_n} \mathrm{Tr}\left\{ G_{ll'}(k) \Delta_i^{\Gamma, \beta}(\boldsymbol{k}) G_{l'l}^{\tau}(-k) \Delta_i^{\dagger \Gamma, \alpha}(\boldsymbol{k}) \right\}$$
$$= \frac{-T_c v^{\Gamma, \alpha}}{N} \sum_{\boldsymbol{k} \sigma \sigma'} \sum_{l_1 l_2} \left[\widetilde{\Delta}_{l',i}^{\Gamma, \beta}(\boldsymbol{k}) \right]_{\substack{l_1 l_2 \\ \sigma \sigma'}} \left[\widetilde{\Delta}_{l,i}^{\Gamma, \alpha}(\boldsymbol{k}) \right]^*_{\substack{l_1 l_2 \\ \sigma \sigma'}}$$
$$\times \frac{\tanh[\beta_c \xi_{l_1, \sigma}(\boldsymbol{k})/2] + \tanh[\beta_c \xi_{l_2, \sigma'}(-\boldsymbol{k})/2]}{2[\xi_{l_1, \sigma}(\boldsymbol{k}) + \xi_{l_2, \sigma'}(-\boldsymbol{k})]}, \quad \text{(A7)}$$

where l, l', l_1, and l_2 are the layer indexes, with $l, l', l_1, l_2 = 1, 2, \ldots, n$; σ, σ' are the spin indexes; and $G_{ll'}(k)$ is the 2×2 Matsubara Green's function for the normal state, which takes the form

$$G_{ll'}(k) = \sum_{l_1} U_{ll_1}(\boldsymbol{k}) [i\omega_n - D_{l_1}(\boldsymbol{k})]^{-1} [U_{l'l_1}(\boldsymbol{k})]^{\dagger}. \quad \text{(A8)}$$

Here $U_{ll'}(\boldsymbol{k})$ is the 2×2 block of the unitary matrix $U(\boldsymbol{k})$, which diagonalizes $H_0(\boldsymbol{k})$: $U^{\dagger}(\boldsymbol{k}) H_0(\boldsymbol{k}) U(\boldsymbol{k}) = D(\boldsymbol{k})$. The $2n \times 2n$ diagonal matrix $D(\boldsymbol{k})$ has the eigenenergies $\xi_j(\boldsymbol{k})$ ($j = 1, 2, \ldots, 2n$) of $H_0(\boldsymbol{k})$ as its diagonal entries. The 2×2 matrix $D_l(\boldsymbol{k})$ is given by

$$D_l(\boldsymbol{k}) = \begin{pmatrix} \xi_{2l-1}(\boldsymbol{k}) & 0 \\ 0 & \xi_{2l}(\boldsymbol{k}) \end{pmatrix},$$

with $\xi_{l,\uparrow}(\boldsymbol{k}) \equiv \xi_{2l-1}(\boldsymbol{k})$, $\xi_{l,\downarrow}(\boldsymbol{k}) \equiv \xi_{2l}(\boldsymbol{k})$. The effective gap matrix $[\widetilde{\Delta}_{l',i}^{\Gamma, \alpha}(\boldsymbol{k})]_{l_1 l_2}$ is defined as

$$\left[\widetilde{\Delta}_{l',i}^{\Gamma, \alpha}(\boldsymbol{k}) \right]_{l_1 l_2} = U_{l'l_1}^{\dagger}(\boldsymbol{k}) \Delta_i^{\Gamma, \alpha}(\boldsymbol{k}) U_{l'l_2}^{*}(-\boldsymbol{k}). \quad \text{(A9)}$$

For a definite IR Γ, if the number of different α is m, then Q is an $nmd^{\Gamma} \times nmd^{\Gamma}$ matrix. Since Q is independent of index i, it is actually a block-diagonalized one, with blocks identical to each other. Therefore, we only have to solve the eigenequation corresponding to the reduced $nm \times nm$ Q matrix and then determine its T_c and eigenstate (the expansion coefficients of the gap function).

Now we demonstrate how to use mirror symmetry to further reduce the Q matrix. We take $n = 2N_0$ (N_0 is an integer) as an example. Only $a_1^{\Gamma, \alpha}, \ldots, a_{N_0}^{\Gamma, \alpha}$ are independent because the mirror symmetry ensures that

$$a_{n+1-l}^{\Gamma, \alpha} = \eta_M \eta^{\Gamma, \alpha} a_l^{\Gamma, \alpha}, \quad \text{(A10)}$$

where $\eta_M = \pm 1$ denotes the mirror parity, while $\eta^{\Gamma, \alpha} = +1(-1)$ for $\psi_i^{\Gamma, \alpha}$ or $\boldsymbol{d}_i^{\Gamma, \alpha} || z (\boldsymbol{d}_i^{\Gamma, \alpha} \perp z)$. Thus, we have

$$a_l^{\Gamma, \alpha} = \sum_{l'=1}^{N_0} \sum_{\beta}^{m} \left(Q_{l,l'}^{\Gamma, \alpha\beta} + \eta_M \eta^{\Gamma, \alpha} Q_{l,n+1-l'}^{\Gamma, \alpha\beta} \right) a_{l'}^{\Gamma, \beta}$$
$$= \sum_{l'=1}^{N_0} \sum_{\beta}^{m} \widetilde{Q}_{l,l'}^{\Gamma, \alpha\beta} a_{l'}^{\Gamma, \beta}, \quad \text{(A11)}$$
$$\widetilde{Q}_{l,l'}^{\Gamma, \alpha\beta} = Q_{l,l'}^{\Gamma, \alpha\beta} + \eta_M \eta^{\Gamma, \beta} Q_{l,n+1-l'}^{\Gamma, \alpha\beta}. \quad \text{(A12)}$$

The reduced $\widetilde{Q}$ is an $N_0 m \times N_0 m$ matrix.

[1] B. Clayman and R. Frindt, Solid State Commun. **9**, 1881 (1971).
[2] H. F. Hess, R. B. Robinson, and J. V. Waszczak, Phys. Rev. Lett. **64**, 2711 (1990).
[3] R. Corcoran, P. Meeson, Y. Onuki, P.-A. Probst, M. Springford, K. Takita, H. Harima, G. Guo, and B. Gyorffy, J. Phys. Condens. Matter **6**, 4479 (1994).
[4] E. Boaknin, M. A. Tanatar, J. Paglione, D. Hawthorn, F. Ronning, R. W. Hill, M. Sutherland, L. Taillefer, J. Sonier, S. M. Hayden, and J. W. Brill, Phys. Rev. Lett. **90**, 117003 (2003).
[5] C. L. Huang, J.-Y. Lin, Y. T. Chang, C. P. Sun, H. Y. Shen, C. C. Chou, H. Berger, T. K. Lee, and H. D. Yang, Phys. Rev. B **76**, 212504 (2007).
[6] C. Berthier, P. Molinié, and D. Jérome, Solid State Commun. **18**, 1393 (1976).
[7] H. Mutka, Phys. Rev. B **28**, 2855 (1983).
[8] A. H. Castro Neto, Phys. Rev. Lett. **86**, 4382 (2001).
[9] T. Yokoya, T. Kiss, A. Chainani, S. Shin, M. Nohara, and H. Takagi, Science **294**, 2518 (2001).
[10] Z.-J. Yao, J.-X. Li, and Z. D. Wang, Phys. Rev. B **74**, 212507 (2006).
[11] I. Guillamón, H. Suderow, J. G. Rodrigo, S. Vieira, P. Rodiere, L. Cario, E. Navarro-Moratalla, C. Martí-Gastaldo, and E. Coronado, New J. Phys. **13**, 103020 (2011).
[12] X. Xi, L. Zhao, Z. Wang, H. Berger, L. Forró, J. Shan, and K. F. Mak, Nat. Nanotechnol. **10**, 765 (2015).
[13] D. Xiao, G.-B. Liu, W. Feng, X. Xu, and W. Yao, Phys. Rev. Lett. **108**, 196802 (2012).
[14] H.-Z. Lu, W. Yao, D. Xiao, and S.-Q. Shen, Phys. Rev. Lett. **110**, 016806 (2013).
[15] R. Suzuki, M. Sakano, Y. Zhang, R. Akashi, D. Morikawa, A. Harasawa, K. Yaji, K. Kuroda, K. Miyamoto, T. Okuda *et al.*, Nat. Nanotechnol. **9**, 611 (2014).
[16] L. Bawden, S. Cooil, F. Mazzola, J. Riley, L. Collins-McIntyre, V. Sunko, K. Hunvik, M. Leandersson, C. Polley, T. Balasubramanian *et al.*, Nat. Commun. **7**, 11711 (2016).
[17] Z. Wu, S. Xu, H. Lu, A. Khamoshi, G. B. Liu, T. Han, Y. Wu, J. Lin, G. Long, and Y. He, Nat. Commun. **7**, 12955 (2016).

[18] P. Dey, L. Yang, C. Robert, G. Wang, B. Urbaszek, X. Marie, and S. A. Crooker, Phys. Rev. Lett. **119**, 137401 (2017).

[19] S. Wu, J. S. Ross, G.-B. Liu, G. Aivazian, A. Jones, Z. Fei, W. Zhu, D. Xiao, W. Yao, D. Cobden *et al.*, Nat. Phys. **9**, 149 (2013).

[20] K. F. Mak, K. L. McGill, J. Park, and P. L. McEuen, Science **344**, 1489 (2014).

[21] M. Tahir, A. Manchon, and U. Schwingenschlögl, Phys. Rev. B **90**, 125438 (2014).

[22] J. Lee, K. F. Mak, and J. Shan, Nat. Nanotechnol. **11**, 421 (2016).

[23] T. Yu and M. W. Wu, Phys. Rev. B **93**, 045414 (2016).

[24] J. M. Lu, O. Zheliuk, I. Leermakers, N. F. Q. Yuan, U. Zeitler K. T. Law, and J. T. Ye, Science **350**, 1353 (2015).

[25] X. Xi, Z. Wang, W. Zhao, J.-H. Park, K. Tuen Law, H. Berger, L. Forró, J. Shan, and K. Mak, Nat. Phys. **12**, 139 (2015).

[26] Y. Saito, Y. Nakamura, M. S. Bahramy, Y. Kohama, J. Ye, Y. Kasahara, Y. Nakagawa, M. Onga, M. Tokunaga, T. Nojima *et al.*, Nat. Phys. **12**, 144 (2016).

[27] Y. Xing, K. Zhao, P. Shan, F. Zheng, Y. Zhang, H. Fu, Y. Liu, M. Tian, C. Xi, H. Liu, J. Feng, X. Lin, S. Ji, X. Chen, Q.-K. Xue, and J. Wang, Nano Lett. **17**, 6802 (2017).

[28] J. Lu, O. Zheliuk, Q. Chen, I. Leermakers, N. E. Hussey, U. Zeitler, and J. Ye, Proc. Natl. Acad. Sci. USA **115**, 3551 (2018).

[29] S. C. Barrera, M. R. Sinko, D. P. Gopalan, N. Sivadas, K. L. Seyler, K. Watanabe, T. Taniguchi, A. W. Tsen, X. Xu, D. Xiao *et al.*, Nat. Commun. **9**, 1427 (2018).

[30] N. F. Q. Yuan, K. F. Mak, and K. T. Law, Phys. Rev. Lett. **113**, 097001 (2014).

[31] B. T. Zhou, N. F. Q. Yuan, H.-L. Jiang, and K. T. Law, Phys. Rev. B **93**, 180501(R) (2016).

[32] G. Sharma and S. Tewari, Phys. Rev. B **94**, 094515 (2016).

[33] Y.-T. Hsu, A. Vaezi, M. H. Fischer, and E.-A. Kim, Nat. Commun. **8**, 14985 (2017).

[34] D. Möckli and M. Khodas, Phys. Rev. B **98**, 144518 (2018).

[35] E. Sohn, X. Xi, W.-Y. He, S. Jiang, Z. Wang, K. Kang, J.-H. Park, H. Berger, L. Forró, K. T. Law *et al.*, Nat. Mater. **17**, 504 (2018).

[36] W.-Y. He, B. T. Zhou, J. J. He, N. F. Yuan, T. Zhang, and K. Law, Commun. Phys. **1**, 40 (2018).

[37] D. Möckli and M. Khodas, Phys. Rev. B **99**, 180505(R) (2019).

[38] J. A. Galvis, L. Chirolli, I. Guillamón, S. Vieira, E. Navarro-Moratalla, E. Coronado, H. Suderow, and F. Guinea, Phys. Rev. B **89**, 224512 (2014).

[39] E. Navarro-Moratalla, J. Island, S. Mañas-Valero, E. Pinilla-Cienfuegos, A. Castellanos-Gomez, J. Quereda, G. Rubio-Bollinger, L. Chirolli, J. Silva-Guillén, N. Agraït *et al.*, Nat. Commun. **7**, 11043 (2016).

[40] Y. Yang, S. Fang, V. Fatemi, J. Ruhman, E. Navarro-Moratalla, K. Watanabe, T. Taniguchi, E. Kaxiras, and P. Jarillo-Herrero, Phys. Rev. B **98**, 035203 (2018).

[41] T. Dvir, F. Massee, L. Attias, M. Khodas, M. Aprili, C. H. L. Quay, and H. Steinberg, Nat. Commun. **9**, 598 (2018).

[42] Y. Ge and A. Y. Liu, Phys. Rev. B **86**, 104101 (2012).

[43] Y. Noat, J. A. Silva-Guillén, T. Cren, V. Cherkez, C. Brun, S. Pons, F. Debontridder, D. Roditchev, W. Sacks, L. Cario, P. Ordejón, A. García, and E. Canadell, Phys. Rev. B **92**, 134510 (2015).

[44] C. Heil, S. Poncé, H. Lambert, M. Schlipf, E. R. Margine, and F. Giustino, Phys. Rev. Lett. **119**, 087003 (2017).

[45] C. E. Sanders, M. Dendzik, A. S. Ngankeu, A. Eich, A. Bruix, M. Bianchi, J. A. Miwa, B. Hammer, A. A. Khajetoorians, and P. Hofmann, Phys. Rev. B **94**, 081404(R) (2016).

[46] J. Zhao, K. Wijayaratne, A. Butler, J. Yang, C. D. Malliakas, D. Y. Chung, D. Louca, M. G. Kanatzidis, J. van Wezel, and U. Chatterjee, Phys. Rev. B **96**, 125103 (2017).

[47] S. J. Youn, M. H. Fischer, S. H. Rhim, M. Sigrist, and D. F. Agterberg, Phys. Rev. B **85**, 220505(R) (2012).

[48] J. Goryo, M. H. Fischer, and M. Sigrist, Phys. Rev. B **86**, 100507(R) (2012).

[49] C.-X. Liu, Phys. Rev. Lett. **118**, 087001 (2017).

[50] Y. Mizukami, H. Shishido, T. Shibauchi, M. Shimozawa, S. Yasumoto, D. Watanabe, M. Yamashita, H. Ikeda, T. Terashima, H. Kontani *et al.*, Nat. Phys. **7**, 849 (2011).

[51] S. K. Goh, Y. Mizukami, H. Shishido, D. Watanabe, S. Yasumoto, M. Shimozawa, M. Yamashita, T. Terashima, Y. Yanase, T. Shibauchi, A. I. Buzdin, and Y. Matsuda, Phys. Rev. Lett. **109**, 157006 (2012).

[52] M. Shimozawa, S. K. Goh, R. Endo, R. Kobayashi, T. Watashige, Y. Mizukami, H. Ikeda, H. Shishido, Y. Yanase, T. Terashima, T. Shibauchi, and Y. Matsuda, Phys. Rev. Lett. **112**, 156404 (2014).

[53] M. Sigrist and K. Ueda, Rev. Mod. Phys. **63**, 239 (1991).

[54] T. Yoshida, M. Sigrist, and Y. Yanase, Phys. Rev. Lett. **115**, 027001 (2015).

[55] F. Zhang, C. L. Kane, and E. J. Mele, Phys. Rev. Lett. **111**, 056403 (2013).

[56] Y. Tanaka, Y. Mizuno, T. Yokoyama, K. Yada, and M. Sato, Phys. Rev. Lett. **105**, 097002 (2010).

[57] L. Fang, Y. Wang, P. Y. Zou, L. Tang, Z. Xu, H. Chen, C. Dong, L. Shan, and H. H. Wen, Phys. Rev. B **72**, 014534 (2005).

[58] K. E. Wagner, E. Morosan, Y. S. Hor, J. Tao, Y. Zhu, T. Sanders, T. M. McQueen, H. W. Zandbergen, A. J. Williams, D. V. West, and R. J. Cava, Phys. Rev. B **78**, 104520 (2008).

[59] O. R. Albertini, A. Y. Liu, and M. Calandra, Phys. Rev. B **95**, 235121 (2017).

[60] C.-S. Lian, C. Si, J. Wu, and W. Duan, Phys. Rev. B **96**, 235426 (2017).

[61] X. Xi, H. Berger, L. Forró, J. Shan, and K. F. Mak, Phys. Rev. Lett. **117**, 106801 (2016).

[62] H. Suderow, V. G. Tissen, J. P. Brison, J. L. Martínez, and S. Vieira, Phys. Rev. Lett. **95**, 117006 (2005).

[63] V. G. Tissen, M. R. Osorio, J. P. Brison, N. M. Nemes, M. García-Hernández, L. Cario, P. Rodière, S. Vieira, and H. Suderow, Phys. Rev. B **87**, 134502 (2013).

[64] D. C. Freitas, P. Rodière, M. R. Osorio, E. Navarro-Moratalla, N. M. Nemes, V. G. Tissen, L. Cario, E. Coronado, M. García-Hernández, S. Vieira, M. Núñez-Regueiro, and H. Suderow, Phys. Rev. B **93**, 184512 (2016).

[65] R. Grasset, Y. Gallais, A. Sacuto, M. Cazayous, S. Mañas-Valero, E. Coronado, and M.-A. Méasson, Phys. Rev. Lett. **122**, 127001 (2019).